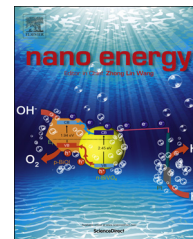




Available online at [www.sciencedirect.com](http://www.sciencedirect.com)

ScienceDirect

journal homepage: [www.elsevier.com/locate/nanoenergy](http://www.elsevier.com/locate/nanoenergy)



COMMUNICATION

# Self-supported yolk-shell nanocolloids towards high capacitance and excellent cycling performance



Ting Zhu<sup>a</sup>, Jing Wang<sup>a</sup>, Ghim Wei Ho<sup>a,b,c,\*</sup>

<sup>a</sup>Department of Electrical and Computer Engineering, National University of Singapore, 4 Engineering Drive 3, 117583 Singapore

<sup>b</sup>Engineering Science Programme, National University of Singapore, 9 Engineering Drive 1, 117575 Singapore

<sup>c</sup>Institute of Materials Research and Engineering, A\*STAR (Agency for Science, Technology and Research), 3 Research Link, 117602 Singapore

Received 25 August 2015; received in revised form 14 October 2015; accepted 28 October 2015  
Available online 7 November 2015

## KEYWORDS

Yolk-shell;  
NiCo<sub>2</sub>S<sub>4</sub>;  
Nanosheets;  
Supercapacitors

## Abstract

To maximize the electrochemical performance of a pseudocapacitor, we have holistically designed yolk-shell nanostructured electrode materials endowed with multiple electroactive redox states, fast redox kinetics and most importantly superior cycling stability. This can effectively be achieved by concoction of high surface area ultrathin mesoporous shell, volumetric buffering void space and lastly an in-built supporting framework that alleviates prevalent fracturing due to prolong cycling. Herein, a polystyrene spheres (PS) core known for its low-cost, lightweight, durability and elastoplasticity properties are explicitly introduced as a localized mechanical support to augment the susceptible ultrathin hollow structures. Unlike conventional physical support which comes directly from a backbone scaffold such as foam, here the yolk-shell structure adopts comparative advantages of void spaces and movable cores needed not only for volumetric buffering but also to assume a self-supporting framework. The PS supported NiCo<sub>2</sub>S<sub>4</sub> (PS@NiCo<sub>2</sub>S<sub>4</sub>) nanocolloids possess high surface area (220-266 m<sup>2</sup> g<sup>-1</sup>) and structural stability which manifested high capacitance and excellent cycling performances.

© 2015 Elsevier Ltd. All rights reserved.

## Introduction

The global warming and the exhausting fossil fuels have greatly changed the energy consumption in human life [1-3]. In the

\*Corresponding author.

E-mail address: [elehgw@nus.edu.sg](mailto:elehgw@nus.edu.sg) (G.W. Ho).

recent decades, some of the sustainable energy sources, such as solar, wind and tidal energies have received intensive research attentions due to their inexhaustible sources and environmental friendliness [4,5]. However, the inconsistency of these energy sources makes it necessary for people to capture and store those energies efficiently to meet the demands of the new rising electrical and electronic devices, ranging from mobile phones, laptops to hybrid electric vehicles [6]. Lithium ion batteries and supercapacitors are the two most commonly studied systems for the energy storage in the past several years [7-9]. The former has been considered to be the best choice for many years in terms of its good performance with high energy density and long-lasting power supply, but the slow power delivery or uptake restricts their application in the rapid growth power market [9,10]. Compared to its counterpart, the latter supercapacitors are drawing increasing research interests due to their much higher power density and longer cycle life, which makes supercapacitor an important component in complementing or replacing batteries in the next few years [11-13]. As supercapacitors are electrochemical devices which are highly dependent on various constituents such as electrodes, electrolyte and separators [7,14,15], hence it is highly desirable to explore novel nanostructured electrode materials for manufacturing high-performance supercapacitors [16].

Transitional metal based materials have received intensive research attentions for supercapacitors as they can deliver much higher capacitance compared to the traditional carbon materials due to the Faradaic mechanism involved which store and release the energy by reversible redox reactions [17-19]. NiCo<sub>2</sub>S<sub>4</sub> is a low-cost binary transitional metal sulfide which exhibits superior electronic conductivity and electrochemical activity compared to the single component of NiS<sub>x</sub> or CoS<sub>x</sub> [20]. By combination of both nickel and cobalt, NiCo<sub>2</sub>S<sub>4</sub> can offer richer redox reactions in much the same way as NiCo<sub>2</sub>O<sub>4</sub> [21]. Compared to single component sulfide material (eg. NiS<sub>x</sub>, CoS<sub>x</sub>) of hollow structures, limited research involved the preparation of NiCo<sub>2</sub>S<sub>4</sub> ternary sulfide materials that takes after a mesoporous yolk-shell structure. The notable synergistic effect between the mesoporous structures and the hollow yolk-shell framework is that they collectively provide a large surface area and pore volume for exceptional accessibility, considerable electroactive sites and fast electron-transport access [22,23]. Yet, the cycling instability of such vulnerable hollow mesoporous structure resulting from structural alteration/degradation is a major hurdle to prolong application [24,25]. Therefore it is rational to introduce a supporting cores serving as mechanical cushion to sustain the entire core-shell structures. Other challenge faced is that yolk-shell materials fabricated by typical Kirkendall or Ostwald ripening processes are limited to yolk-shell structures of similar core and shell compositions. Furthermore, there is inadequate control over the wall thickness and shell structure which yields random and bulky structures of low surface area that compromises diffusivity of the electrolyte into the interior structure. Hence it is desirable to fabricate mesoporous and permeable electroactive shells with chemically and mechanically stable supporting cores to improve the electrochemical performances for the next-generation supercapacitors [26].

Herein, we report a PS core and ultrathin NiCo<sub>2</sub>S<sub>4</sub> mesoporous nanosheets shell with distinctive core@void@shell configuration. The PS core is exclusively chosen due to its attractive attributes such as low-cost, lightweight, durability, chemical inertness and more importantly its elastoplasticity properties. The yolk-shell

nanosheets structure presents a permeable mesoporous shells that renders the entrapped PS movable in the confined hollow space infiltrated with the electrolyte, which could endow the system a fast charge transfer kinetics [27]. Essentially, the elastoplastic PS core to uphold the ultrathin hollow nanosheets framework and hence acting as localized mechanical support. Unlike, physical support which comes directly from a backbone scaffold such as foam, here the yolk-shell structure adopts comparative advantages of void spaces and movable cores needed not only for volumetric buffering but also to assume a self-supporting framework. The as-prepared PS@NiCo<sub>2</sub>S<sub>4</sub> yolk-shell nanocolloids possess a well-defined ultrathin mesoporous structure of high surface area (>200 m<sup>2</sup> g<sup>-1</sup>). In virtue of the PS core as in-built support, the designed electrodes have shown high specific capacitance with excellent cycling performances. Furthermore, the developed material is validated to fuel an LED as an asymmetrical supercapacitor device, hence exhibiting the potential use as a high-performance supercapacitor.

## Experimental

### Synthesis of PS@m-SiO<sub>2</sub>

The preparation of PS@m-SiO<sub>2</sub> nanocolloids is based on a modified Stöber method described elsewhere [28]. Briefly, 26 mg of PS spheres and 0.1 g of hexadecyltrimethylammonium bromide (CTAB) were dispersed into 7 mL of DI water and 40 mL of isopropanol (IPA) by ultrasonication for 15 min at room temperature (RT). Then 1 mL of ammonia aqueous solution (wt%=25%) was added into the mixture under magnetic stirring followed by the addition of 0.2 mL of Tetraethyl Orthosilicate (TEOS). The mixture was further stirred at RT for 3 h before the white products were washed by DI-water and ethanol several times and collected by centrifugation. The collected products were dried at 60 °C in an air-flow oven for 24 h for the further usage.

### Synthesis of PS@m-SiO<sub>2</sub>@NiCo-Silicate

In the typical synthesis, 20 mg of the as-prepared PS@m-SiO<sub>2</sub> nanocolloids was dispersed into 40 mL of DI-water by ultrasonication for 20 min, followed by the addition of 0.5 g of urea for the activation of the SiO<sub>2</sub> surface. After sonication for another 5 min, 0.2 mL of Ni(NO<sub>3</sub>)<sub>2</sub> (0.1 M) and 0.4 mL of Co(NO<sub>3</sub>)<sub>2</sub> (0.1 M) were added dropwise into the solution. Sample I and II are derived from molar ratio (MR) of Ni<sup>2+</sup> and Co<sup>2+</sup>, MR=1 and 2 respectively. The mixture was sealed in a glass bottle and shaken by hands for 2 min before heated at 90 °C in an air-flow oven for 12 h. The reaction was allowed to cool down naturally and the products are collected by the rinse-centrifugation process with DI water and ethanol several times.

### Preparation of PS@NiCo<sub>2</sub>S<sub>4</sub> yolk-shell structures

In order to prepare yolk-shell PS@NiCo<sub>2</sub>S<sub>4</sub>, 10 mg of the as-prepared PS@m-SiO<sub>2</sub>@NiCo-Silicate was first dispersed into a mixture of 5 mL DI-water and 25 mL ethanol by sonication for 10 min. Later, 80 mg of thiourea was added into the solution and the mixture was transferred into Teflon and sealed in an autoclave before heated at 105 °C for 18 h.

After the reaction, the black products were collected by the rinse-centrifugation process with DI-water and ethanol several times. The obtained products were dried thoroughly at 60 °C in a vacuum oven for 12 h.

### Materials characterizations

All the samples were characterized by field-emission scanning electron microscopy (FESEM, JEOL FEG JSM-7001F)

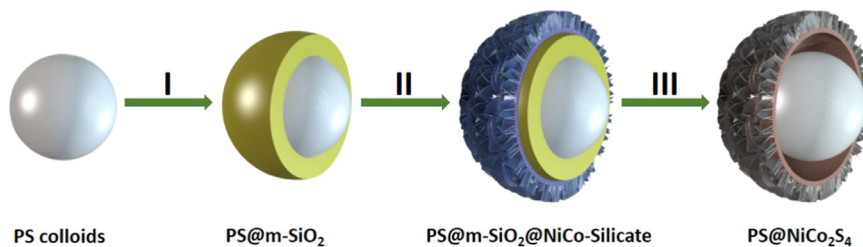


Fig. 1 Schematic illustration of the formation process of the PS@NiCo<sub>2</sub>S<sub>4</sub> yolk-shell nanocolloids.

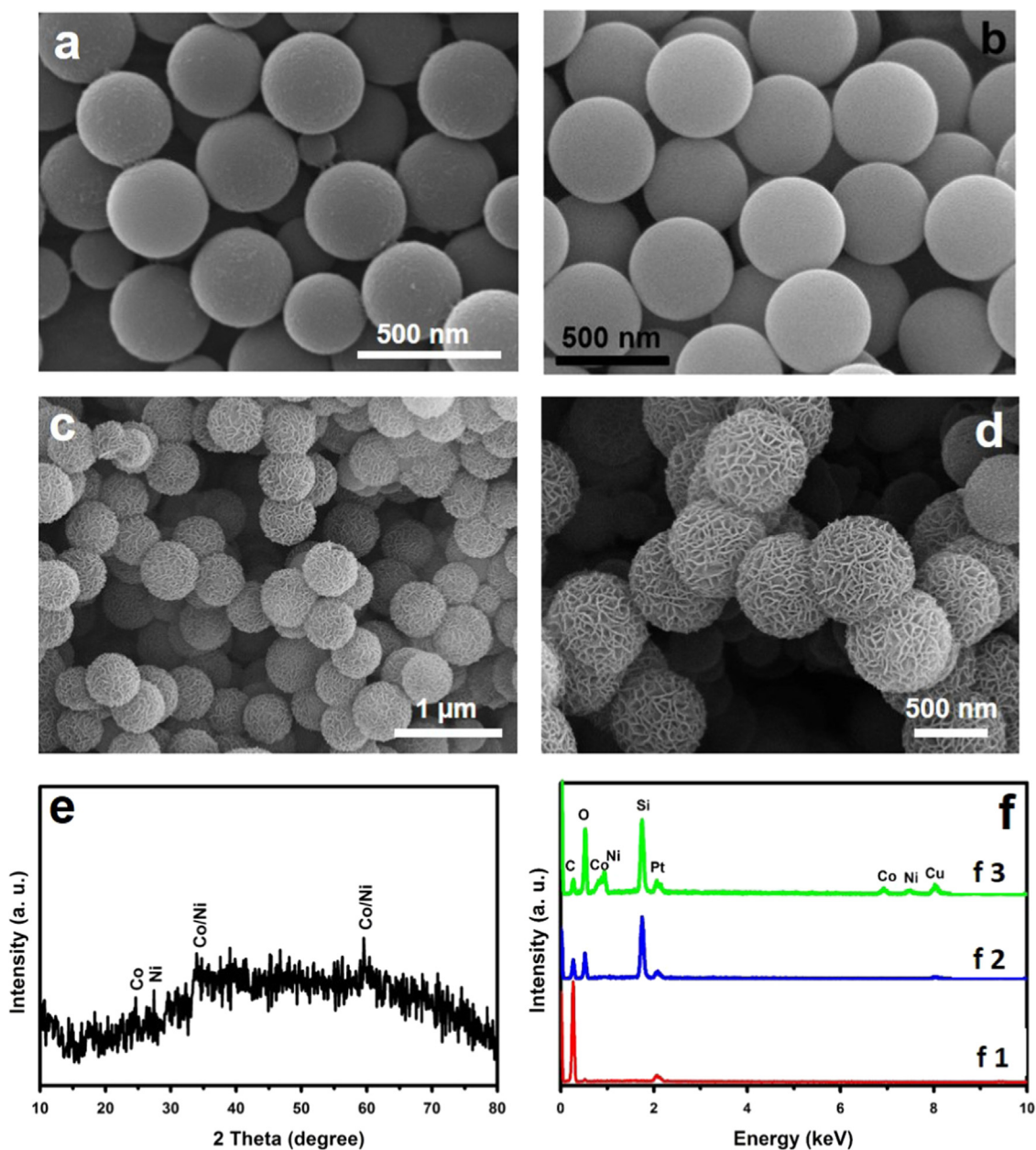


Fig. 2 FESEM images (a, b, c and d), XRD pattern (e) and EDX results (f) of PS spheres (a, f1), PS@SiO<sub>2</sub> (b, f2) and the typical PS@SiO<sub>2</sub>@NiCo-Silicate (c, d, e and f3).

equipped with an energy dispersive X-ray spectroscopy (EDX), transmission electron microscopy (TEM, Philips FEG CM300) and X-ray diffraction (XRD, Philips X-ray diffractometer, Cu Ka). The texture properties of the relevant samples were carried out at 77 K with a Quantachrome NOVA-1200 system using Brunauer, Emmett and Teller (BET) method.

### Electrochemical measurements

The working electrodes were prepared by mixing the 80 wt% of electroactive material (PS@NiCo<sub>2</sub>S<sub>4</sub>), 10 wt% of carbon black, and 10 wt% of polyvinylidene difluoride (PVDF, Aldrich). The slurry was then pressed onto metal Ni foams, and dried thoroughly at 60 °C in vacuum. The electrolyte used was a 2 M of KOH aqueous solution. The electrochemical performances including CV, GCCD and EIS (frequency ranging from 0.01-100 KHz with 5 mV amplitude) of the individual electrodes were evaluated on a CHI 660D electrochemical workstation using cyclic voltammetry and chronopotentiometry tests with a three-electrode cell where Pt foil served as the counter electrode and a standard calomel electrode (SCE) as the reference electrode.

### Assembly of PS@NiCo<sub>2</sub>S<sub>4</sub> /CNTs asymmetrical supercapacitors

The asymmetrical supercapacitor full cells (5 cm × 4 cm) were assembled using two pieces of nickel foams loaded with PS@NiCo<sub>2</sub>S<sub>4</sub> and carbon nanotubes (CNTs), respectively. The two electrodes were packed with Al foil using an electrolyte-soaked (2 M KOH) separator in between. The mass of the active materials in the two electrodes have been calculated beforehand based on the charge balance to maximize the energy density of the cells.

### Results and discussion

Fig. 1 presents the synthetic route of the yolk-shell PS@NiCo<sub>2</sub>S<sub>4</sub> nanocolloids. Firstly, the PS spheres are employed as hard templates for fine coating of m-SiO<sub>2</sub> using a modified Stöber method. Next, Nickel-Cobalt Silicates are grown onto the PS@m-SiO<sub>2</sub> to form PS@m-SiO<sub>2</sub>@NiCo-Silicate with hierarchical shells. By controlling the molar ratio (MR) of Ni<sup>2+</sup> and Co<sup>2+</sup>, the hierarchical shells of the grown NiCo-Silicate can be tuned (MR=1; 2). Finally, hydrothermal sulfurization process is carried out to convert the silicate shells into sulfide in the presence of thiourea and simultaneously

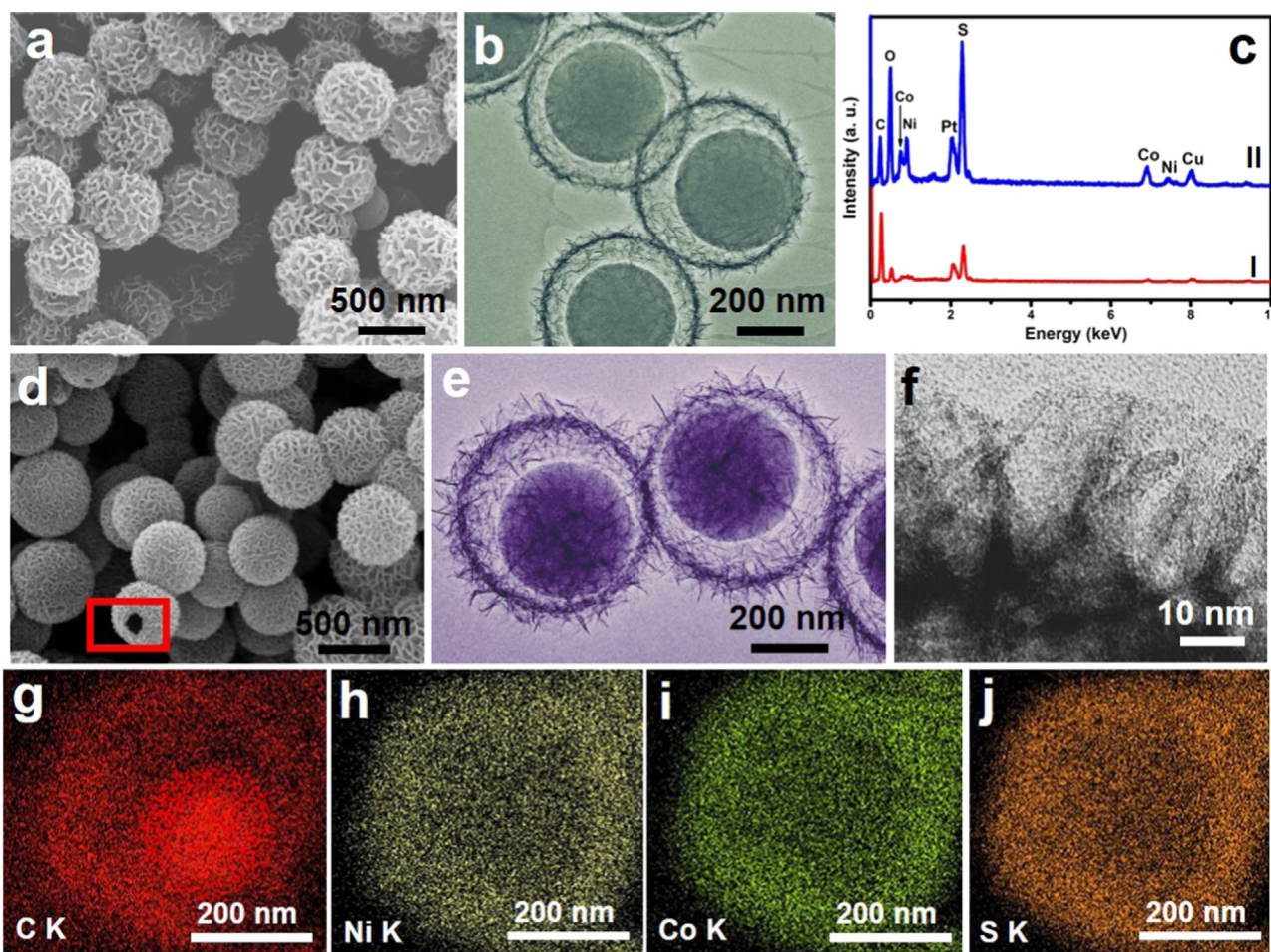


**Fig. 3** FESEM (a, d), TEM (b, e and f), EDX patterns (c) and TEM elemental mappings (g-j) of the as-prepared PS@NiCo<sub>2</sub>S<sub>4</sub> yolk-shell nanocolloids (Sample I: a-c; Sample II: c-j).

removes the sandwiched  $m\text{-SiO}_2$ . This leads to the formation of porous  $\text{NiCo}_2\text{S}_4$  shells with “rattle-like” movable PS cores. As a result, integrated ultrathin mesoporous shell, void space and in-built PS supported nanocolloids are fabricated by this effective one-arrow-two-hawks method.

After silica coating, the surface of the PS spheres (Fig. 2a) becomes smooth and the diameters are increased from 350 nm to 450 nm ( $\text{PS@m-SiO}_2$ , Fig. 2b), indicating a coating thickness of  $\sim 50$  nm. In addition, the EDX results before (Fig. 2-f1) and after (Fig. 2-f2) silica coating implied the successful deposition of silica onto the PS spheres. The Cu and Pt peaks in Fig. f are attributed to the Cu substrate and Pt sputtering before FESEM characterization. The uniform growth of NiCo-Silicate hierarchical shells onto the  $\text{PS@m-SiO}_2$  is confirmed by the FESEM shown in Fig. 2c-d (sample with  $\text{MR}=2$ ). The particle sizes of the  $\text{PS@m-SiO}_2\text{@NiCo-Silicate}$  are enlarged from 450 nm to 480 nm, and the silicate shells are observed to be composed of hierarchical nanosheets. XRD (Fig. 2e) and EDX (Fig. 2-f3) are performed to determine the crystallographic phases and chemical composition of the obtained particles. All the XRD peaks can be assigned to the nickel and cobalt silicate although very weak peaks can be observed due to the low crystallinity [29]. Further EDX analyses have confirmed the presence of Ni and Co in the products as well as the sharp peak of Si.

After sulfurization by hydrothermal process in the presence of thiourea, the NiCo-Silicate shells are completely converted to  $\text{NiCo}_2\text{S}_4$  with well-retained hierarchical structures (Fig. 3a (sample I) and d (sample II)). The hollow structures of the obtained sulfurized samples are confirmed by the FESEM (the broken hole indicated by the red rectangle in Fig. 3d). TEM analyses affirm the core@void@shell configuration of a yolk-shell structure for both samples as shown in Fig. 3b and e. It can be observed clearly that the PS are well preserved without distinct shrinkage or distortion in both samples, indicating their chemical inertness towards the hydrothermal sulfurization. Notably, sample II which is grown based on higher MR precursor shows appreciable increased in nanosheets formation than sample I. Higher resolution TEM image of Fig. 3f shows the nanosheets are composed of ultrathin and mesoporous structures. The chemical compositions of the two samples are further examined by EDX patterns (Fig. 3c). The peaks of C, O, Ni and Co are detected for both samples. The presence of sharp peaks of S and absence of Si peak have affirmed the complete conversion of silicate species to sulfide products. The extraneous Pt and Cu come from the sputtering process and sample substrate used for FESEM characterization, respectively. TEM elemental mappings are also performed to examine the element

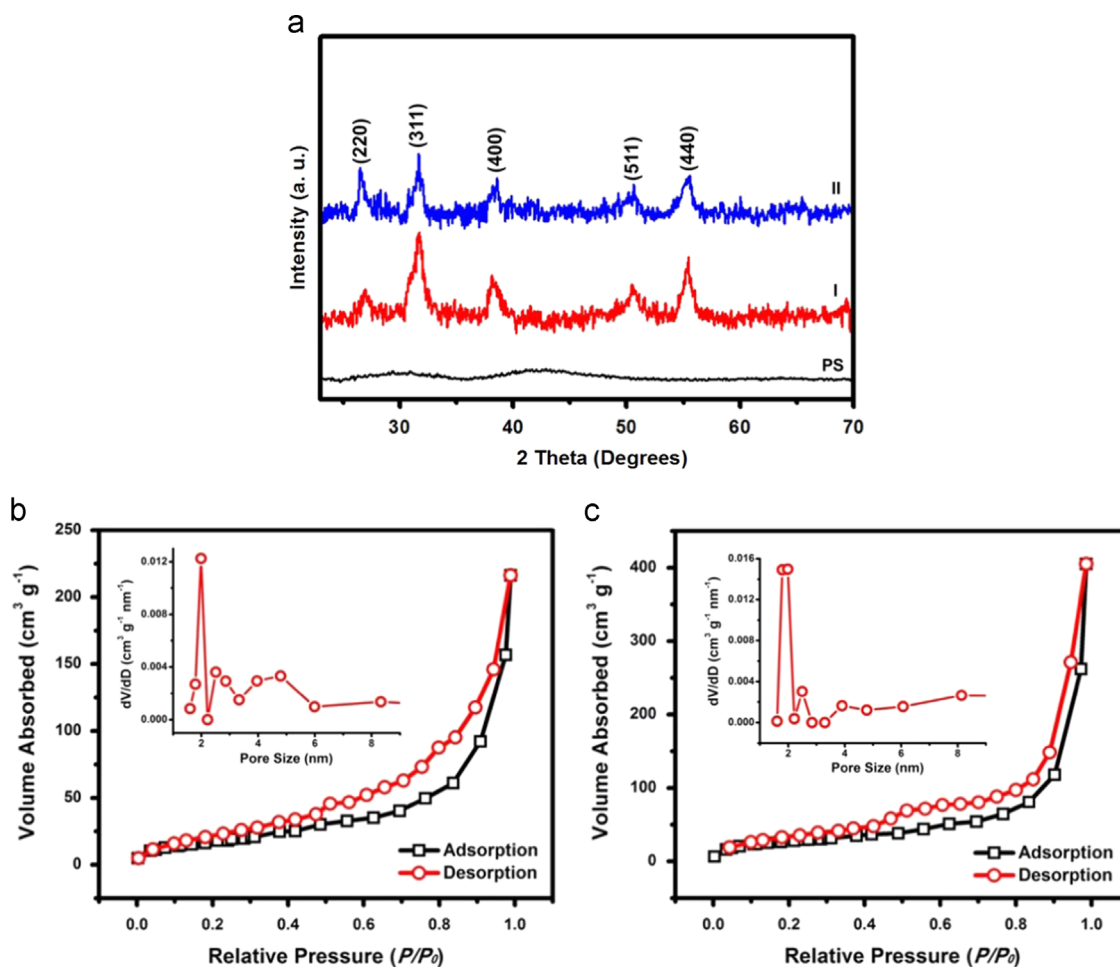
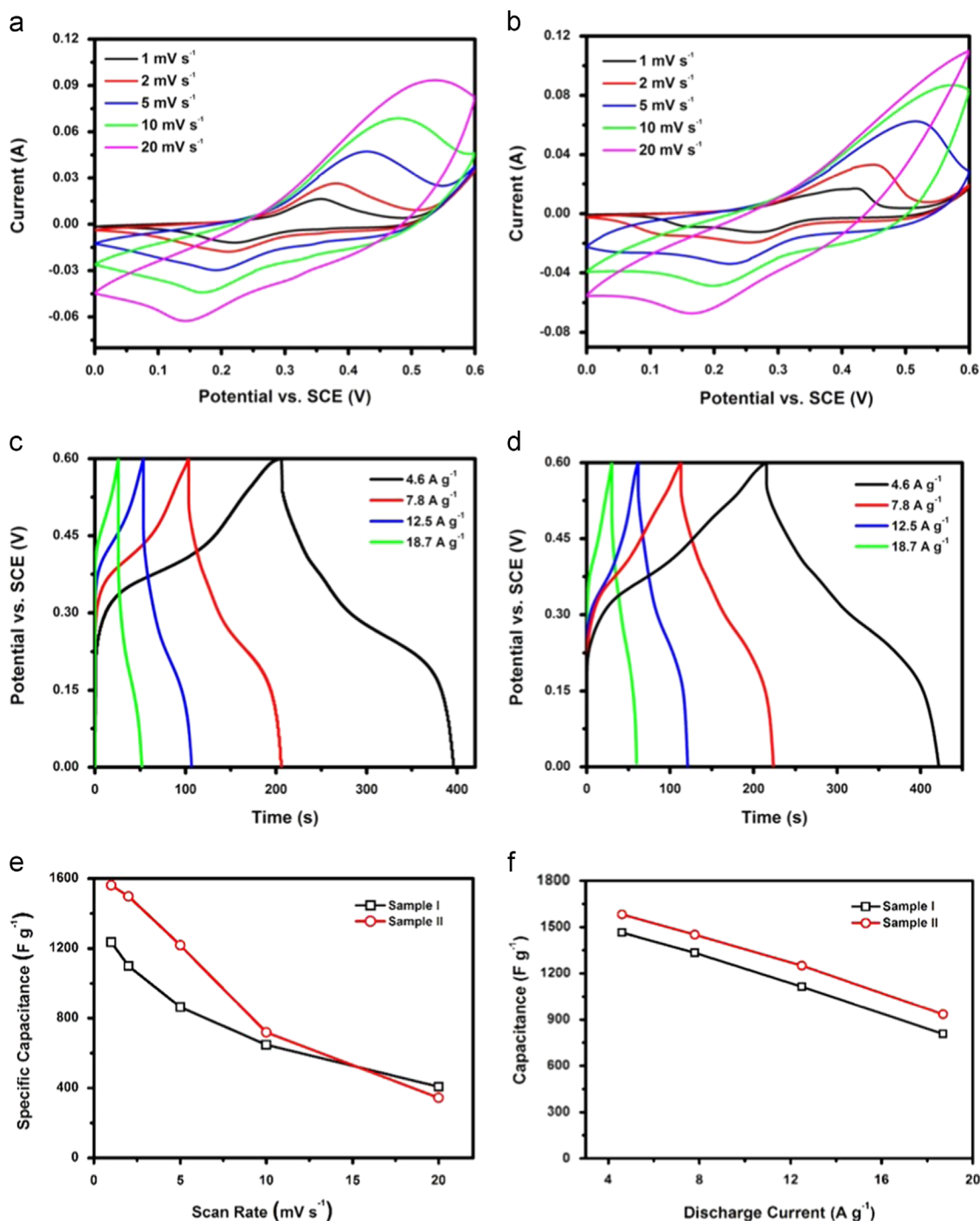


Fig. 4 XRD patterns of the as-prepared  $\text{PS@NiCo}_2\text{S}_4$  samples I, II and pure PS spheres (a) BET results of the  $\text{PS@NiCo}_2\text{S}_4$  sample I (b) and II (c), and the insets show the corresponding pore size distributions obtained from desorption isotherms.



**Fig. 5** CV (a, b) and GCCD curves (c, d) performed at different scan rates and current densities with a same voltage window of 0–0.6 V (vs. SCE) of the PS@NiCo<sub>2</sub>S<sub>4</sub> sample I (a, c) and II (b, d); specific capacitances calculated from the corresponding different scan rates (e) and current densities (f) for both of the two samples.

distributions for sample II (Fig. 3g–j). The C, Ni, Co and S elements revealed from the mapping results are consistent with previous TEM findings, which confirm the obtained PS cores with nickel-cobalt-sulfide shells.

In order to study the crystallography of the as-obtained PS supported sulfide materials, XRD is employed to determine the crystal phases (Fig. 4a). All the indexed peaks can be assigned to NiCo<sub>2</sub>S<sub>4</sub> (JCPDS No. 20-0782) [30]. Pure PS spheres are also

examined and no obvious XRD peaks can be picked out, which shows the purity of the as-derived sulfide materials. The as-prepared PS@NiCo<sub>2</sub>S<sub>4</sub> nanocolloids are expected to hold large surface area in virtue of their ultrathin mesoporous nanosheets and hollow structures. Therefore BET characterization is carried out using the N<sub>2</sub> adsorption/desorption measurement at 77 K (Fig. 4b–c). The two samples have a similar pore sizes distribution of ~2 nm, which can be seen in the insets of Fig. 4b–c,

respectively. Furthermore, sample I possesses a large specific surface area of  $220 \text{ m}^2 \text{ g}^{-1}$  associated to its highly porous nanosheets and hollow structures. Evidently, a higher specific surface area of  $266 \text{ m}^2 \text{ g}^{-1}$  was registered for sample II, possibly due to increase nanosheets shell providing more adsorption sites. The high surface areas with microporous structures shown herein for the two samples offer increase electroactive sites for improved electrochemical performances [31].

The as-derived PS supported  $\text{NiCo}_2\text{S}_4$  porous materials are evaluated as electrodes for supercapacitors. The redox reactions involved during the charge and discharge process can be described as follows [32,33]:

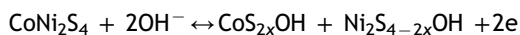


Fig. 5a-b show the CV curves obtained from different scan rates (1-20  $\text{mV s}^{-1}$ ) with a voltage window of 0-0.6 V (vs. SCE) for both samples. Two pairs of broadened peaks can be observed from the CV curves, which are associated with the Faradaic redox reactions related to the Ni and Co, exhibiting pseudo-capacitive property of the materials [34,35]. The average specific capacitances of the samples can be calculated from the CV curves based on the following equation [36]:

$$C = \frac{1}{mu(V_2 - V_1)} \int_{V_1}^{V_2} I(V) dV$$

Where  $C$  ( $\text{F g}^{-1}$ ) is the specific capacitance,  $m$  (g) is the mass of the active material,  $I$  (A) is the current,  $u$  ( $\text{V s}^{-1}$ ) is the CV scan rate,  $V_1$  and  $V_2$  (V) are the voltage cuts during the CV scanning.

The average specific capacitances of the two samples calculated from different scan rates are displayed in Fig. 5e. Specific capacitances of 1236, 1100, 864, 648, and  $408 \text{ F g}^{-1}$  can be calculated at scan rates of 1, 2, 5, 10 and  $20 \text{ mV s}^{-1}$  for sample I. With higher specific surface area and richer cobalt content, the sample II has delivered much higher capacitances of 1561, 1498, 1219 and  $719 \text{ F g}^{-1}$  at 1, 2, 5,  $10 \text{ mV s}^{-1}$ , respectively except for a lower capacitance of  $344 \text{ F g}^{-1}$  at  $20 \text{ mV s}^{-1}$ . The specific capacitances are also evaluated and compared by the galvanostatic charge-discharge measurements. The charge-discharge curves performed at various current densities are presented in Fig. 5c-d. The plateaus observed at 0.15-0.45 V (vs. SCE) for both samples imply their pseudo-capacitive property, which is consistent with the CV scanning results. At current densities of 4.6, 7.8, 12.5, and  $18.7 \text{ A g}^{-1}$ , capacitances of 1464, 1334, 1113, and  $807 \text{ F g}^{-1}$  are attained by sample I. While sample II, higher capacitances of 1582, 1451, 1250, and  $934 \text{ F g}^{-1}$  are obtained at corresponding current densities (Fig. 5f). The reported capacitances for both samples herein are attributed to the high surface areas, well-defined mesoporous yolk-shell structures, and high electrochemical activity of the multiple nickel cobalt sulfide electroactive redox chemistry. The specific capacitance registered at  $4.6 \text{ A g}^{-1}$  of sample II is  $1582 \text{ F g}^{-1}$ , is higher than that of the reported  $\text{NiCo}_2\text{S}_4$  nanosheets arrays and nanoplates [21].

The cycling capability is also important in supercapacitors for any commercial applications, and hence prolonged cycles are conducted at a medium current density ( $7.8 \text{ A g}^{-1}$ ) with results exhibited in Fig. 6a. It can be seen from the curves that both samples experienced a slight capacitance increase during the first 500 cycles before stabilization. After 3000 cycles, the specific capacitances are recorded at  $1384 \text{ F g}^{-1}$  and  $1481 \text{ F g}^{-1}$  for sample I and II,

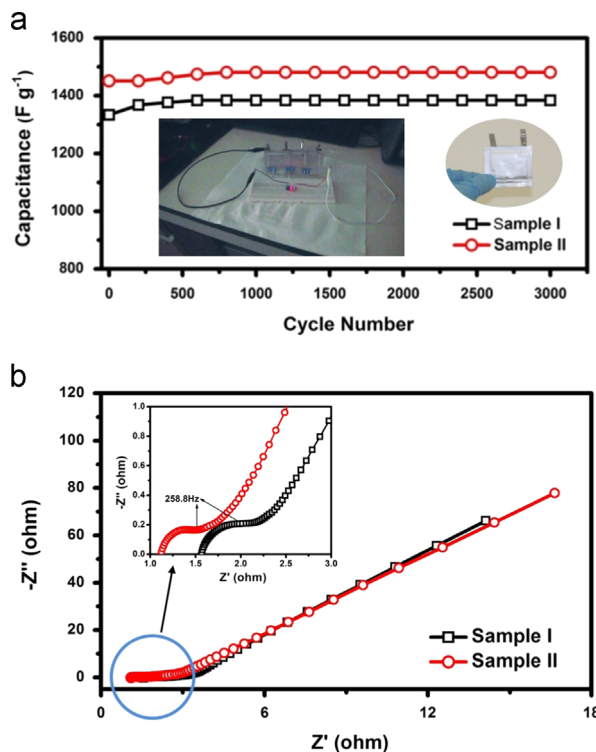
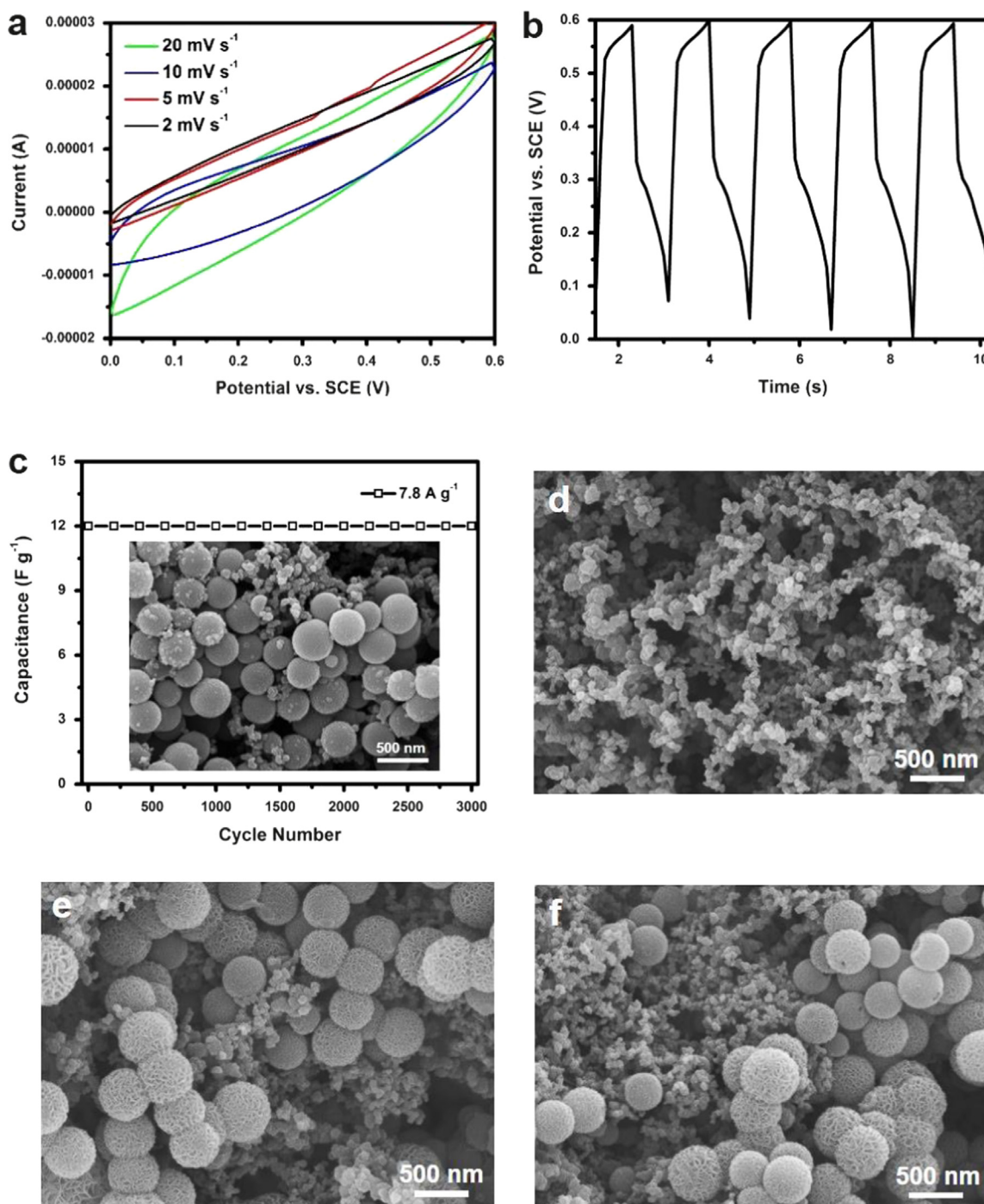


Fig. 6 Cycling performances up to 3000 cycles performed at  $7.8 \text{ A g}^{-1}$  (a) and Nyquist plots of both of the two samples (b). The inset in (a, left) shows a LED is fueled by the fabricated asymmetric supercapacitors (a, right).

respectively, showing their excellent cycling stability. The excellent cycling performances is attributed to core@void@shell configuration, where PS core is exclusively introduced due to its befitting attributes such as economical, lightweight, durable, fairly chemically inert and more importantly its elastoplasticity property as a localized mechanical support to counteract the susceptible ultrathin hollow structures. The yolk-shell nanosheets structure presents a permeable mesoporous shell that allows electrolyte accessibility such that the entrapped cores are immersed/surrounded with fluid which render its mobility within the confined hollow space [37]. The elastoplastic PS core move about freely to actively administer the mechanical support needed to hold the ultrathin hollow nanosheets framework.

The EIS analysis for both of the two samples were carried out in the frequency range from 0.01 to 100 KHz at open circuit potential (0 V) with 5 mV amplitude (Nyquist plots shown in Fig. 6b). The first intersections of Nyquist plots on the  $Z'$  axis in the high-frequency region reveal the high-frequency equivalent series resistance of capacitors ( $R_s$ ) which are contributed by the ohmic resistance of the electrolyte, the internal resistance of electrode materials, and contact resistance between electrodes and current collectors [38]. While the semicircles crossing high and mid-frequency are attributed to the charge-transfer resistance, which has been enlarged and shown in the inset of Fig. 6b. The lower  $R_s$  together with the smaller radius of sample II than sample I can generally show a lower impedance and better electric conductivity for sample II, leading to a better electrochemical performance than sample I [39]. For the asymmetric supercapacitor cells, the slurry of the sample II is packed into full cells using carbon nanotubes



**Fig. 7** CV curves (a), first five GCCD curves (b) and cycling performance (c) of the pure PS spheres. SEM images (inset in c, d-f) of the pure PS spheres (inset in c, after 3000 cycles), carbon black (d), sample I (e) and sample II (f) after being cycled for 3000 times.

(CNTs) as counter electrodes. An as-fabricated cell is shown in the insets of Fig. 6a (right), and then three cells are connected in series to form a closed circuit to fuel a LED (inset in Fig. 6a, left). Our result has shown that the connected cells can fuel an LED after the cells are charged to 3.8 V, showing the potential commercialization for the next-generation supercapacitors.

In order to rule out the capacitance contribution from the PS spheres, CV and GCCD tests of the pure PS spheres are also carried out and the results are shown in Fig. 7. No redox

reaction peaks are observed from the CV curves (Fig. 7a) while no obvious Faradaic plateaus can be seen in charge-discharge process (Fig. 7b), showing the non-electrochemical activity of the pure PS spheres. In addition, the cycling test at the same current density ( $7.8 \text{ A g}^{-1}$ ) also shows a very low ( $12 \text{ F g}^{-1}$ ) but stable specific capacitance up to 3000 cycles (Fig. 7c), which indicates that the PS spheres play a crucial and main role as an in-built physical support for the  $\text{NiCo}_2\text{S}_4$  ultrathin shell structure and contributed to less than 1.5% of the total

capacitance. In addition, the morphology of PS spheres along with carbon black (the smaller particles added to improve the electrode conductivity) after prolong cycling is shown in Fig. 7c inset indicate their robustness and durability as mechanical support. Also, the morphology of carbon black nanoparticles and electrode materials for sample I and II after 3000 cycles are examined by SEM characterizations, respectively, as shown in Fig. 7d-f. The structures of PS@NiCo<sub>2</sub>S<sub>4</sub> spheres shown in Fig. 7e (sample I) and Fig. 7f (sample II) were well preserved after being cycled for 3000 times, which manifests the structural stability of the as-fabricated hybrid nanocolloids.

## Conclusion

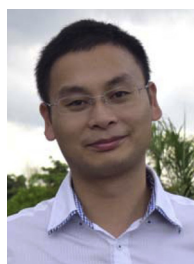
In summary, yolk-shell NiCo<sub>2</sub>S<sub>4</sub> nanocolloids are prepared through a facile template-engaged method and then used as electrode materials for supercapacitors. The hierarchical shells can be tuned by controlling the molar ratios between Ni and Co, while the PS cores herein are served as localized mechanical support for sustaining prolong cycling. The obtained electrochemical results have shown high specific capacitances with excellent cycling stability after comparing with some of the previous work. The asymmetrical supercapacitor full cells are also fabricated using CNTs and the as-prepared PS@NiCo<sub>2</sub>S<sub>4</sub> as the positive and negative electrodes, and the connected full cells are able to fuel a LED after charged to 3.8 V by an external power supply, showing the potential application as a next-generation supercapacitor.

## Acknowledgments

This work is supported by MOE R-263-000-B38-112 and R-263-000-B63-112.

## References

- [1] C. Liu, F. Li, L.P. Ma, H.M. Cheng, *Adv. Mater.* 22 (2010) E28-E62.
- [2] K. Maeda, K. Teramura, D.L. Lu, T. Takata, N. Saito, Y. Inoue, K. Domen, *Nature* 440 (2006) 295.
- [3] Y.Q. Qu, X.F. Duan, *Chem. Soc. Rev.* 42 (2013) 2568-2580.
- [4] D.M. Schultz, T.P. Yoon, *Science* 343 (2014) 985-993.
- [5] M.G. Walter, E.L. Warren, J.R. McKone, S.W. Boettcher, Q. X. Mi, E.A. Santori, N.S. Lewis, *Chem. Rev.* 110 (2010) 6446-6473.
- [6] P. Simon, Y. Gogotsi, *Nat. Mater.* 7 (2008) 845-854.
- [7] M. Winter, R.J. Brodd, *Chem. Rev.* 104 (2004) 4245-4269.
- [8] G.H. Yu, X. Xie, L.J. Pan, Z.N. Bao, Y. Cui, *Nano Energy* 2 (2013) 213-234.
- [9] S.L. Candelaria, Y.Y. Shao, W. Zhou, X.L. Li, J. Xiao, J. G. Zhang, Y. Wang, J. Liu, J.H. Li, G.Z. Cao, *Nano Energy* 1 (2012) 195-220.
- [10] A.S. Arico, P. Bruce, B. Scrosati, J.M. Tarascon, W. Van Schalkwijk, *Nat. Mater.* 4 (2005) 366-377.
- [11] L.L. Zhang, X.S. Zhao, *Chem. Soc. Rev.* 38 (2009) 2520-2531.
- [12] J.R. Miller, P. Simon, *Science* 321 (2008) 651-652.
- [13] S.J. Ding, T. Zhu, J.S. Chen, Z.Y. Wang, C.L. Yuan, X.W. Lou, *J. Mater. Chem.* 21 (2011) 6602-6606.
- [14] G.Q. Zhang, L. Yu, H.E. Hoster, X.W. Lou, *Nanoscale* 5 (2013) 877-881.
- [15] X. Xiao, X. Peng, H.Y. Jin, T.Q. Li, C.C. Zhang, B. Gao, B. Hu, K. F. Huo, J. Zhou, *Adv. Mater.* 25 (2013) 5091-5097.
- [16] R.R. Salunkhe, J.J. Lin, V. Malgras, S.X. Dou, J.H. Kim, Y. Yamauchi, *Nano Energy* 11 (2015) 211-218.
- [17] L. Yang, S. Cheng, Y. Ding, X.B. Zhu, Z.L. Wang, M.L. Liu, *Nano Lett.* 12 (2012) 321-325.
- [18] G.Q. Zhang, H.B. Wu, H.E. Hoster, M.B. Chan-Park, X.W. Lou, *Energy Environ. Sci.* 5 (2012) 9453-9456.
- [19] M.K. Liu, W.W. Tjiu, J.S. Pan, C. Zhang, W. Gao, T.X. Liu, *Nanoscale* 6 (2014) 4233-4242.
- [20] Y.F. Zhang, M.Z. Ma, J. Yang, C.C. Sun, H.Q. Su, W. Huang, X. C. Dong, *Nanoscale* 6 (2014) 9824-9830.
- [21] W. Chen, C. Xia, H.N. Alshareef, *ACS Nano* 8 (2014) 9531-9541.
- [22] W.-M. Zhang, J.-S. Hu, Y.-G. Guo, S.-F. Zheng, L.-S. Zhong, W.-G. Song, L.-J. Wan, *Adv. Mater.* 20 (2008) 1160-1165.
- [23] X. Wang, X.-L. Wu, Y.-G. Guo, Y. Zhong, X. Cao, Y. Ma, J. Yao, *Adv. Funct. Mater.* 20 (2010) 1680-1686.
- [24] R. Ghosh Chaudhuri, S. Paria, *Chem. Rev.* 112 (2012) 2373-2433.
- [25] Z. Teng, S. Wang, X. Su, G. Chen, Y. Liu, Z. Luo, W. Luo, Y. Tang, H. Ju, D. Zhao, G. Lu, *Adv. Mater.* 26 (2014) 3741-3747.
- [26] X.Y. Lai, J.E. Halpert, D. Wang, *Energy Environ. Sci.* 5 (2012) 5604-5618.
- [27] J.Y. Wang, N.L. Yang, H.J. Tang, Z.H. Dong, Q. Jin, M. Yang, D. Kisailus, H.J. Zhao, Z.Y. Tang, D. Wang, *Angew. Chem.-Int. Ed.* 52 (2013) 6417-6420.
- [28] Y. Lu, J. McLellan, Y.N. Xia, *Langmuir* 20 (2004) 3464-3470.
- [29] J. Qu, W. Li, C.Y. Cao, X.J. Yin, L. Zhao, J. Bai, Z. Qin, W. G. Song, *J. Mater. Chem.* 22 (2012) 17222-17226.
- [30] R.J. Zou, Z.Y. Zhang, M.F. Yuen, J.Q. Hu, C.S. Lee, W.J. Zhang, *Sci. Rep.* 5 (2015) 7.
- [31] C. Largeot, C. Portet, J. Chmiola, P.-L. Taberna, Y. Gogotsi, P. Simon, *J. Am. Chem. Soc.* 130 (2008) 2730-2731.
- [32] J.W. Xiao, L. Wan, S.H. Yang, F. Xiao, S. Wang, *Nano Lett.* 14 (2014) 831-838.
- [33] W. Hu, R.Q. Chen, W. Xie, L.L. Zou, N. Qin, D.H. Bao, *ACS Appl. Mater. Interfaces* 6 (2014) 19318-19326.
- [34] H.L. Wang, Q.M. Gao, L. Jiang, *Small* 7 (2011) 2454-2459.
- [35] T.Y. Wei, C.H. Chen, H.C. Chien, S.Y. Lu, C.C. Hu, *Adv. Mater.* 22 (2010) 347-351.
- [36] C.H. An, Y.J. Wang, Y.A. Huang, Y.A. Xu, C.C. Xu, L.F. Jiao, H. T. Yuan, *Crystengcomm* 16 (2014) 385-392.
- [37] J. Liu, S.Z. Qiao, J.S. Chen, X.W. Lou, X.R. Xing, G.Q. Lu, *Chem. Commun.* 47 (2011) 12578-12591.
- [38] M.D. Stoller, S.J. Park, Y.W. Zhu, J.H. An, R.S. Ruoff, *Nano Lett.* 8 (2008) 3498-3502.
- [39] J.M. Shen, A.D. Liu, Y. Tu, G.S. Foo, C.B. Yeo, M.B. Chan-Park, R.R. Jiang, Y. Chen, *Energy Environ. Sci.* 4 (2011) 4220-4229.



Dr Ting Zhu received his B. Eng. in Chemistry of Materials (2007) and M. Eng. in Biomedical Engineering (2010) from Sichuan University, China. Then he obtained his Ph. D. degree from Nanyang Technological University, Singapore in 2014 and now working as a research fellow at the National University of Singapore. His research interest is in the development of nanostructured materials for applications in energy conversion and storage.



**Dr Jing Wang** received his B.Sc. degree in Chemistry Engineering and Technology from Nanjing Tech University in 2007 and then Ph.D. degree in Chemical Engineering in 2012. He is currently a research fellow at the National University of Singapore (NUS). His research interests include nanofabrication and photocatalysis.



**Prof. Ghim Wei Ho** received her Ph.D. on semiconductor nanostructures at the Nanoscience Centre, University of Cambridge in 2006. She is an Associate Professor of the Department of Electrical & Computer Engineering at the National University of Singapore (NUS). She is also one of the pioneer associates of the Engineering Science Programme (ESP) at NUS. Her research thrusts are centred around the development of nanostructured materials for photovoltaic applications and nanomaterials for photocatalytic applications.